Supporting Information

Jadhao et al. 10.1073/pnas.1413986111

SI Text

Evaluation of the Force on a Vertex Due to Bending

The free energy of our model membrane comprises bending, stretching, and electrostatic energies. As we adopt a molecular dynamics simulation method as the basis of minimizing the free energy, the energy expression does not suffice (as it would for example in case of a Monte Carlo simulation of the membrane). We require analytical expressions for the gradients of the energy with respect to the vertex positions. Whereas the evaluation of the gradient of stretching and electrostatic energy terms is straightforward, computing the gradient of the bending term involves some key steps that we highlight here.

We begin with a summary of our discretized membrane model. We work with a membrane that is a 2D, closed surface that is embedded in three dimensions, and it has spherical topology. We model the membrane as a mesh of discrete points that are assumed to form a triangular lattice. We call the discrete point a vertex. The basic unit of the discretized membrane is a triangle that is identified by three vertices, three edges, and one face. Each edge has exactly two vertices and two adjoining faces, and each face has exactly three vertices and three edges.

Consider a face identified by the index k with vertices v_0, v_1, v_2, which have the respective position vectors $\mathbf{r}_0$, $\mathbf{r}_1$ and $\mathbf{r}_2$, where the vectors are being defined with respect to an origin that is chosen arbitrarily. We define relative position vectors $\mathbf{r}_{ij} = \mathbf{r}_i - \mathbf{r}_j$. The area A_k of the face can be expressed in terms of these relative position vectors as

$$A_k = \frac{1}{2}|\mathbf{r}_{10} \times \mathbf{r}_{20}|. \quad \text{[S1]}$$

Note that A_k is invariant under cyclic permutation of the indices $0 \to 1 \to 2 \to 0$. In other words,

$$A_k = \frac{1}{2}|\mathbf{r}_{10} \times \mathbf{r}_{20}| = \frac{1}{2}|\mathbf{r}_{21} \times \mathbf{r}_{01}| = \frac{1}{2}|\mathbf{r}_{02} \times \mathbf{r}_{12}|. \quad \text{[S2]}$$

Finally, the normal vector associated with the kth face can be written as

$$\hat{\mathbf{n}}_k = \frac{\mathbf{r}_{20} \times \mathbf{r}_{21}}{|\mathbf{r}_{20} \times \mathbf{r}_{21}|}. \quad \text{[S3]}$$

Using the definition of area A_k, we can also write the normal vector as

$$\hat{\mathbf{n}}_k = \frac{\mathbf{r}_{20} \times \mathbf{r}_{21}}{2A_k}. \quad \text{[S4]}$$

To simulate the bending of the membrane, we use the following discretized form for the bending energy:

$$U_B = \frac{\kappa}{2}\sum_{e \in \mathrm{E}} |\hat{\mathbf{n}}_{e,1} - \hat{\mathbf{n}}_{e,2}|^2, \quad \text{[S5]}$$

which forms the first term in Eq. **1**. Here, $\hat{\mathbf{n}}_{e,1}$ and $\hat{\mathbf{n}}_{e,2}$ are normals to the two adjacent faces that share the edge e, E is the set of all edges, and κ is a constant related to the bending rigidity of the continuum membrane. We can promptly reduce the above expression to the following:

$$U_B = \kappa \sum_{e \in \mathrm{E}} \left(1 - \hat{\mathbf{n}}_{e,1} \cdot \hat{\mathbf{n}}_{e,2}\right). \quad \text{[S6]}$$

The bending force $\mathbf{f}_i$ on a vertex v_i is the negative gradient of U_B at $\mathbf{r}_i$, where $\mathbf{r}_i$ is the position vector of the vertex v_i. It is easy to see from the above equation that $\mathbf{f}_i$ is

$$\mathbf{f}_i = \kappa \nabla_{\mathbf{r}_i} \sum_{e \in \mathrm{E}} \hat{\mathbf{n}}_{e,1} \cdot \hat{\mathbf{n}}_{e,2}. \quad \text{[S7]}$$

We now describe the procedure used to compute the bending force $\mathbf{f}_i$. The sum in Eq. **S7** is over all of the edges of the discretized membrane. Because the gradient of a sum is the sum of the gradients, it suffices to show the process for the gradient computation for one edge, the final result for the gradient can be arrived at by repeating the procedure for all of the other edges and consolidating the gradient evaluations. Consider an edge e and let us identify the faces that share this edge with indices k and l. Let $\hat{\mathbf{n}}_k$ and $\hat{\mathbf{n}}_l$ be respectively the normals associated with faces k and l. Further, let us associate the face k with vertices v_0, v_1, and v_2. With no loss of generality, we identify vertices v_0, v_2, and v_3 to face l (recall that faces k and l are neighbors). Clearly, the edge between v_0 and v_2 is the shared edge (Fig. S1). We define $\mathbf{r}_0$, $\mathbf{r}_1$, $\mathbf{r}_2$, and $\mathbf{r}_3$, respectively, as the position vectors of v_0, v_1, v_2, and v_3. It should be evident that $\hat{\mathbf{n}}_k \cdot \hat{\mathbf{n}}_l$ is a function of the position vectors of all of the four vertices. If the vertex v_i is not one of these four vertices, the contribution to the force $\mathbf{f}_i$ from this edge vanishes. Further, it is not difficult to see that the expression for the gradient with respect to the (position vector of) vertex v_i when v_i is one of the vertices that lied on the shared edge e ($v_i = v_0$ or $v_i = v_2$) is different from the gradient expression for the vertex v_i which is not on the shared edge ($v_i = v_1$ or $v_i = v_3$). From symmetry considerations, the result for the gradient with respect to $\mathbf{r}_0$ leads to the expression for the gradient at the v_2 vertex. Similarly, the gradient expression for the v_3 vertex is obtained from the result for the gradient with respect to vertex $\mathbf{r}_1$. Thus, we only need to perform two gradient calculations explicitly.

It is useful to define a scalar s as

$$s = (\mathbf{r}_{20} \times \mathbf{r}_{21}) \cdot (\mathbf{r}_{20} \times \mathbf{r}_{32}), \quad \text{[S8]}$$

with which we can write

$$\hat{\mathbf{n}}_k \cdot \hat{\mathbf{n}}_l = \frac{s}{4A_kA_l}. \quad \text{[S9]}$$

It is easy to show that the gradient in the above expression takes the form

$$\nabla\left(\hat{\mathbf{n}}_k \cdot \hat{\mathbf{n}}_l\right) = \frac{1}{4A_kA_l}\left(\nabla s - s\left(\frac{\nabla A_k}{A_k} + \frac{\nabla A_l}{A_l}\right)\right). \quad \text{[S10]}$$

The gradient of s, A_k, and A_l can be readily evaluated from Eqs. **S8** and **S1** with respect to $\mathbf{r}_0$ and $\mathbf{r}_1$. These gradient evaluations allow us to first calculate the gradient of $\hat{\mathbf{n}}_k \cdot \hat{\mathbf{n}}_l$ with respect $\mathbf{r}_0$ following Eq. **S10**. Switching indices 0 and 2 in the resulting expression and multiplying the result by a negative sign leads to the expression for the gradient of $\hat{\mathbf{n}}_k \cdot \hat{\mathbf{n}}_l$ with respect to $\mathbf{r}_2$. Next, we compute the gradient of $\hat{\mathbf{n}}_k \cdot \hat{\mathbf{n}}_l$ with respect to $\mathbf{r}_1$. Switching indices 1 and 3 in the resulting expression and multiplying the result by

a negative sign leads to the expression for the gradient of $\hat{\mathbf{n}}_k \cdot \hat{\mathbf{n}}_l$ with respect to $\mathbf{r}_3$. This completes the evaluation of the contribution from the edge e toward the bending force on a vertex v_i.

Analysis of Shape Transitions in Charged Shells

In the main text, we simulate a closed soft shell with a fixed amount of charge uniformly distributed on the surface. We let the charges interact via a screened (Debye–Hückel) potential field which can be tuned, and allow only those deformations to the shape of the shell that preserve the enclosed volume. The initial shell conformation is set to be spherical. Our key finding is that upon increasing the strength of the electrostatic interactions, either by increasing the Debye length or enhancing the charge z associated with a discretized vertex on the shell, the shape of the shell changes. In general, the shape transition obeys the order spheres → ellipsoids → discs → bowls, and we have demonstrated that the shape change is driven by the reduction of electrostatic energy. For some cases, the parameter range to observe the full spectrum of the aforesaid shapes is too narrow and we see a sphere directly changing into bowl-shaped structures. In the main text, we also provided explanations for the origin of observed shape transitions which were substantiated by analytical calculations resulting from the consideration of the deformation of a charged spherical shell into oblate spheroidal shells of varying eccentricity. Here we provide the details of the analytical calculations.

The explanation provided in the main text for the observed transitions is as follows. Due to the mutual repulsion between the surface charges, the shell seeks to expand and stretch. Because the volume enclosed in the shell must remain fixed, the shell increases its area to lower its electrostatic energy. However, an increase of area costs in stretching (and to a lesser extent, bending) energy. The competition between the stretching and electrostatic energy sets an effective area for the membrane, which the latter must conform to. The salt concentration c controls this competition, and hence the area assigned, thus leading to the formation of a variety of shapes, including discs and bowls. We test this explanation by performing analytical calculations for the following simpler version of our simulation system. We focus on the initial half of the observed shape transition sphere → ellipsoid → disc. Judging by the simulation snapshots (Fig. 1), we approximate these shapes as oblate spheroids with different degrees of eccentricity e and major semiaxis lengths a. Because the volume of the shell is fixed, we realize that e and a are coupled and our simplified model shell can be characterized by a single parameter which we choose to be e. The competition between elastic and electrostatic energies can now be considered as determining the eccentricity e for the oblate spheroid. The concentration c, which in the original simulation served as a control over the area of the membrane, can now be considered as tuning the eccentricity. In other words, the lowering of c can be understood as an increase in e for the oblate spheroid. Thus, we set out to examine the behavior of the electrostatic energy of an oblate spheroidal shell as its eccentricity is changed.

Because an exact calculation of the electrostatic energy of an oblate spheroidal shell with Debye–Hückel type of charge–charge interaction is more cumbersome, we invoke another approximation and examine the pure Coulomb energy of a uniformly charged oblate spheroidal shell. Because we also observe shape transitions by varying the charge strength of the shell at a fixed concentration (which can assume a low value), computing the bare Coulomb interaction result does have a direct relevance to our simulation findings. We will often, as an example to compare back to our simulation results, refer to the particular shape transition observed for the shell represented by bending rigidity of $\kappa = 10$ and $z = 0.6$. This transition is recorded in the shell snapshots belonging to the right column in Fig. 1 and next in the open blue circles of Fig. 3. For convenience, we show the snapshots associated with this shape transition at the top of Fig. S2.

We now derive the general expression for the Coulomb energy of a uniformly charged oblate spheroidal shell, which, to the best of our knowledge, is not available in the literature.

Electrostatic Energy of a Uniformly Charged Oblate Spheroidal Shell. An ellipsoid is described by the equation

$$\frac{x^2}{a_1^2}+\frac{y^2}{a_2^2}+\frac{z^2}{a_3^2}=1, \qquad \text{[S11]}$$

where a_1, a_2, and a_3 are the semiprincipal lengths associated with the three Cartesian axes. A spheroid is an ellipsoid whose cross-section normal to the z axis (the choice of the axis is arbitrary) is a circle (rather than an ellipse). An oblate spheroid is a spheroid where $a_1 = a_2 > a_3$. The following is an equation that generates an oblate spheroid:

$$\frac{r^2}{a_1^2}+\frac{z^2}{a_3^2}=1, \qquad \text{[S12]}$$

where $r=\sqrt{x^2+y^2}$ is the distance between the point on the surface of the spheroid and the z axis. It is convenient to define the eccentricity e as

$$e=\sqrt{1-\frac{a_3^2}{a_1^2}}. \qquad \text{[S13]}$$

Note that $0 < e < 1$ for an oblate spheroid. When $e \to 0$, the oblate spheroid reduces to a sphere. In the opposite limit of $e \to 1$, one obtains a circular disc. We will invoke these limits at several places in what follows. Also, from here forward, we will identify $a_1 = a$.

First we consider oblate spheroidal coordinates u, v, ϕ, which are related to the Cartesian coordinates x, y, and z by

$$x = ae\cosh(u)\sin(v)\cos(\phi), \qquad \text{[S14]}$$

$$y = ae\cosh(u)\sin(v)\sin(\phi), \qquad \text{[S15]}$$

$$z = ae\sinh(u)\cos(v), \qquad \text{[S16]}$$

where

$$0 \le u < \infty, \quad 0 \le v \le \pi, \quad -\pi < \phi \le \pi. \qquad \text{[S17]}$$

The set (u, v, ϕ) uniquely characterizes a point in the 3D space. It is straightforward to show that the metric coefficients are

$$h_u = h_v = ae\sqrt{\sinh^2 u + \cos^2 v}, \quad h_\phi = ae\cosh u \sin v, \qquad \text{[S18]}$$

with which the form for the Laplacian $\nabla^2\Phi = 0$ is readily obtained. The oblate spheroidal shell in these coordinates is represented by the simple equation $u = u_0$, where u_0 is connected to the eccentricity via the relation

$$\operatorname{sech} u_0 = e. \qquad \text{[S19]}$$

The region of space interior to the spheroid corresponds to the values $0 \le u < u_0$ and the exterior region is represented by the $u > u_0$ domain.

Gaussian units will be used in the following calculation. Our goal is to find the electrostatic potential generated by a uniformly charged oblate shell represented by $u = u_0$. Because this system has

axial symmetry, the electrostatic potential created by the oblate spheroid will depend only on the coordinates u and v. Using separation of variables we can write the solution as $\Phi(u,v) = U(u)V(v)$, upon which the Laplace equation separates into two differential equations for u and v. A closer examination of these equations reveals the general solution for the potential to be

$$\Phi(u,v) = \sum_{n=0}^{\infty} \left(A_n P_n(i\sinh u) + B_n Q_n(i\sinh u)\right) P_n(\cos v), \quad \textbf{[S20]}$$

where P_n and Q_n are Legendre functions of the first and second kind respectively, and A_n and B_n are unknown coefficients. To ensure that the solutions are bounded in the interior and exterior regions of the spheroid, we find that $A_n = 0$ in the domain $u > u_0$, and $B_n = 0$ when $0 < u < u_0$. We thus have the following form for the potential inside and outside the oblate shell:

$$\Phi_{\text{in}} = \sum_{n=0}^{\infty} A_n P_n(i\sinh u) P_n(\cos v), \quad \textbf{[S21]}$$

$$\Phi_{\text{out}} = \sum_{n=0}^{\infty} B_n Q_n(i\sinh u) P_n(\cos v). \quad \textbf{[S22]}$$

The potential must be continuous at the shell surface $u - u_0 = 0$. This boundary condition leads to the relation

$$A_n P_n(i\sinh u_0) = B_n Q_n(i\sinh u_0) \quad \textbf{[S23]}$$

for $n = 0, 1, 2, \ldots$. Note that $\sinh u_0 = (1/e)\sqrt{1-e^2}$. The discontinuity in the normal component of the electric field at the charged surface provides the other boundary condition:

$$-\hat{u}\cdot\nabla\Phi_{\text{out}} + \hat{u}\cdot\nabla\Phi_{\text{in}} = 4\pi\sigma, \quad \textbf{[S24]}$$

where σ is the surface-charge density. Using the expression for the gradient in oblate coordinates, the above equation becomes

$$\frac{1}{h_u}\frac{\delta\Phi_{\text{in}}}{\delta u}\bigg|_{u=u_0} - \frac{1}{h_u}\frac{\delta\Phi_{\text{out}}}{\delta u}\bigg|_{u=u_0} = 4\pi\sigma, \quad \textbf{[S25]}$$

where h_u is given by Eq. **S18**. Using Eqs. **S21** and **S22** in Eq. **S25**, the above boundary condition becomes

$$\sum_{n=0}^{\infty} \left(A_n P_n'(i\sinh u_0) - B_n Q_n'(i\sinh u_0)\right) i\cosh u_0 P_n(\cos v) = 4\pi\sigma a\sqrt{1-e^2\sin^2 v}. \quad \textbf{[S26]}$$

Using Eq. **S23** in Eq. **S26**, we can eliminate B_n in favor of A_n and solve for the latter to obtain

$$A_n = \frac{2n+1}{2} 4\pi\sigma a i\cosh u_0 Q_n(i\sinh u_0) \times \int_0^{\pi} \sqrt{1-e^2\sin^2 v}\, P_n(\cos v)\sin v\, dv, \quad n = 0, 1, \ldots. \quad \textbf{[S27]}$$

In arriving at this result we used the identity

$$W\left(P_n(z), Q_n(z)\right) = \frac{1}{1-z^2}, \quad \textbf{[S28]}$$

where W is the Wronskian of $P_n(z)$ and $Q_n(z)$, and the orthogonality relation for the Legendre polynomials

$$\int_0^{\pi} P_n(\cos v) P_l(\cos v)\sin v\, dv = \frac{2}{2n+1}\delta_{nl}. \quad \textbf{[S29]}$$

It is easily checked that for odd n, the integral in Eq. **S27** vanishes, implying $A_1 = A_3 = A_5 \ldots = 0$. Using A_n in Eq. **S23**, B_n is known as well and consequently from Eqs. **S21** and **S22**, the electrostatic potential can be calculated at any point in space.

For the computation of the electrostatic energy, the knowledge of the potential on the shell surface suffices. Using Eqs. **S21** and **S27**, we obtain the surface potential as

$$\Phi_{\text{shell}}(v,e,a) = 4\pi\sigma a i\cosh u_0 \times \sum_{n=0,2,4,\ldots} \frac{2n+1}{2} Q_n(i\sinh u_0) \times P_n(i\sinh u_0) I_n(e) P_n(\cos v), \quad \textbf{[S30]}$$

where $I_n(e)$ is the integral

$$I_n(e) = \int_0^{\pi} \sqrt{1-e^2\sin^2 v} P_n(\cos v)\sin v dv. \quad \textbf{[S31]}$$

The electrostatic energy is given by the equation

$$U = \frac{1}{2}\int \sigma\Phi_{\text{shell}} d^2 s. \quad \textbf{[S32]}$$

The shell surface area element in the oblate spheroidal coordinates is given by

$$d^2 s = h_v h_\phi\, dv d\phi = a^2\sqrt{1-e^2\sin^2 v}\sin v dv d\phi, \quad \textbf{[S33]}$$

where the second equality follows from Eqs. **S18** and **S19**. After substituting this expression for the area element in Eq. **S32** and using Eq. **S30**, we find the electrostatic energy to be

$$U(e,a,\sigma) = 4\pi^2\sigma^2 a^3 i\cosh u_0 \times \sum_{n=0,2,4,\ldots} \frac{2n+1}{2} Q_n(i\sinh u_0) \times P_n\left(i\sinh u_0\right)\left(I_n(e)\right)^2. \quad \textbf{[S34]}$$

As we consider the shell to have a uniformly distributed total charge Q, it is useful to express the result in terms of Q rather than σ. Using the fact that the area of an oblate spheroid is

$$\mathscr{A}(e,a) = 2\pi a^2 S(e), \quad \textbf{[S35]}$$

where

$$S(e) = 1 + \left(\frac{1}{e} - e\right)\tanh^{-1} e, \quad \textbf{[S36]}$$

we obtain the electrostatic energy of the oblate shell as

$$U(e,a,Q) = \frac{Q^2}{a}\frac{1}{\left(S(e)\right)^2}\frac{i}{e} \times \sum_{n=0,2,4,\ldots} \frac{2n+1}{2} Q_n\left(i\frac{\sqrt{1-e^2}}{e}\right) \times P_n\left(i\frac{\sqrt{1-e^2}}{e}\right)\left(I_n(e)\right)^2. \quad \textbf{[S37]}$$

Note that we have assumed throughout the above derivation that the spheroidal shell is in free space. If the environment surrounding the shell is polarizable, the above result for the energy must be scaled down by the dielectric constant of the environment assuming that the latter can be represented as a uniform dielectric medium.

We now take a quick look at the limiting cases of the energy expression found in Eq. **S37**. First we let e approach zero, which corresponds to a spherical shell, and find

$$U(e\to 0,a,Q)=\frac{Q^2}{2a}. \qquad \textbf{[S38]}$$

Indeed, we recover the well-known result for the energy of a uniformly charged spherical shell. Taking the opposite limit, $e \to 1$, which corresponds to a circular disc, gives

$$U(e\to 1,a,Q;n\le 6)=0.84872\frac{Q^2}{a}, \qquad \textbf{[S39]}$$

where we have included terms up to $n = 6$ in the expansion in Eq. **S37** as the series converges rapidly [in what follows, we will work with the expression of $U(e, a, Q)$ that includes terms up to $n = 6$]. Unlike the spherical case, it is difficult to locate the energy of a uniformly charged disc in the literature. It can, however, be derived using the result for the electrostatic potential on the surface of a disc obtained in ref. 1. Carrying out the derivation, we obtain the electrostatic energy of a uniformly charged disc of radius a and total charge Q as

$$U_{\text{disc}}=\frac{8}{3\pi}\frac{Q^2}{a}. \qquad \textbf{[S40]}$$

We can now compare the disc energy obtained in Eq. **S39** with the above exact result and find the deviation to be

$$\frac{U_{\text{disc}}-U(e\to 1,a,Q;n\le 6)}{U_{\text{disc}}}\times 100\approx 0.01\%. \qquad \textbf{[S41]}$$

Clearly, the two energies are in very good agreement.

Application of Volume Constraint. In our simulations, the shell deforms under the constraint of constant volume. The volume of an oblate spheroid is

$$\Omega(e,a)=\frac{4}{3}\pi a^3\sqrt{1-e^2}. \qquad \textbf{[S42]}$$

This equation suggests that if Ω is fixed, a and e are coupled. The volume of the shell in our simulations is constrained to its initial volume which was taken to be that of the sphere of radius R. Hence, a and e become related via the equation

$$a\equiv a(e,R)=\frac{R}{(1-e^2)^{\frac{1}{6}}}. \qquad \textbf{[S43]}$$

Eliminating a from Eq. **S37**, we arrive at the expression for the electrostatic energy of an oblate spheroidal shell constrained to a fixed volume of $(4/3)\pi R^3$ as a function of the eccentricity e:

$$U(e,R,Q)=l_B\frac{Q^2}{R}\frac{\left(1-e^2\right)^{\frac{1}{6}}}{(S(e))^2}\frac{i}{e}\times\sum_{n=0,2,4,\ldots}\frac{2n+1}{2}Q_n\left(i\frac{\sqrt{1-e^2}}{e}\right)\times P_n\left(i\frac{\sqrt{1-e^2}}{e}\right)\left(I_n(e)\right)^2, \qquad \textbf{[S44]}$$

where we have expressed the final result in a dimensionless form by introducing Bjerrum length l_B (in other words, the energy is measured relative to the thermal energy at room temperature). Note that Q is now the charge in units of electron charge. Because in our simulation we consider the charged shell to be present in an aqueous medium, we take $l_B = 0.714$ nm (the Bjerrum length in water), and we use $R = 10$ nm just as is the case with our simulated system. We define the quantity dU as

$$dU=U(e,R,Q)-U(e\to 0,R,Q), \qquad \textbf{[S45]}$$

which is the energy relative to the electrostatic energy of the sphere with identical parameters.

We now evaluate dU for the case of $Q = 600$ and report its variation with e in Fig. S2. We show the eccentricity e increasing from 0 on the right to 1 on the left, inviting a comparison with Fig. 3 (upper half). It is clearly seen that the energy of an oblate spheroidal shell subject to the constraint of constant volume decreases with increasing e. In other words, a charged shell with an ellipsoid-like shape has lower Coulomb energy than a charged sphere of the same volume, and further, a disc-like shape reduces the Coulomb energy even more. Hence, the order of transitions between these shapes as predicted by our simulations is backed by the above analytical results. Further, we consider the curve followed by the blue open circles in the upper half of Fig. 3 which shows the change in the total electrostatic energy of the shell (relative to the spherical conformation) as the concentration is lowered. This curve corresponds to the case of $Q = 600$ with associated snapshots shown in the top of Fig. S2. Comparison between this curve and the analytical result produced in Fig. S2 shows that our calculations qualitatively agree with the trend captured in our simulations. We note that the level of approximation we have used in these analytical calculations performed for the simplified version of our simulation system does not allow us to make quantitative comparisons.

In Fig. 4 we showed the spatial distribution of electrostatic energy on the surface of a disc (top row) as predicted by our simulations. Our analytical calculations allow us to confirm some of the features of this distribution. Eq. **S30** provides the potential on the surface of the oblate shell characterized by eccentricity e and major semiaxis a as a function of the oblate spheroidal coordinate v. This expression can be quickly converted into a form that complies with the aforementioned constraint of constant volume by using Eq. **S43** to substitute for a in terms of e and R. The local electrostatic potential energy U_L can be defined in terms of the resulting potential as $U_L(v, e) = z\Phi_{\text{shell}}(v, e, R, Q)$, where z is the charge associated with the vertex on the shell and we have suppressed the dependence of U_L on other variables for brevity. In terms of the total charge Q and the number of discretizations N, we have $z = Q/N$. It is easy to show that the local potential energy is

$$U_L(v,e)=l_B\frac{zQ}{R}\frac{1}{S(e)}\frac{i}{e}\times\sum_{n=0,2,4,\ldots}(2n+1)Q_n\left(i\frac{\sqrt{1-e^2}}{e}\right)\times P_n\left(i\frac{\sqrt{1-e^2}}{e}\right)I_n(e)P_n(\cos v). \qquad \textbf{[S46]}$$

This expression can be seen as providing the variation of the potential energy on the surface of the shell. We note that the oblate spheroidal coordinate v measures the deviation of a point from the z axis, $v = 0$ refers to the center of the shell, and $v = \pi/2$ corresponds to the edge. As before, we consider the case of $Q = 600$ (with $z = 0.6$ like in our simulations). We plot the variation of U_L as a function of v for different e. We see that for the spherical shell ($e = 0$), the potential energy is constant everywhere,

which is to be expected. However, as e increases, the energy becomes nonuniform. In particular, for $e = 0.95$, which corresponds to a disc-like shape, we find the electrostatic energy varies significantly with v. It is higher near the center and lower on the edge of the disc. As is evident from the top row of Fig. 4, we observe this trend in our simulation results as well.

The Effect of Counterion Condensation on Shell Shape

In the main text we report the shapes that minimize the free energy of a soft, uniformly charged shell present in an aqueous medium with salt. Because the shell is charged, the surrounding solvent contains counterions in addition to the salt ions. We assumed that the counterions remain in the bulk and do not condense on the shell surface. However, in a real system or in an experiment it is possible that a fraction of the counterions do condense, and in that event it becomes important to analyze their effect on the observed shape transitions. In this section, we present a calculation based on the Manning–Oosawa two-state model (2, 3) that qualitatively captures this effect (4, 5). We consider a Wigner–Seitz (WS) cell of volume $V_{\rm WS}$ containing a single shell, with $Q = zN$ charge on its surface, placed at the center. The cell also contains N counterions, each of charge z to neutralize the shell charge and we consider a salt-free system for simplicity. The counterions are separated into two distinct groups: free ions and condensed ions. The condensed counterions are restricted to have translational motion in a thin layer of volume $V = 2\pi a^2 S(e) b$ surrounding the shell, where b is the thickness of the layer. Free ions occupy the available space in the WS cell, which in the dilute limit can be approximated to be the volume of the cell. We focus our arguments on the sphere-to-oblate transition using the analytical results derived in the previous section, although the procedure outlined below can be applied to study other (disc → bowl) transitions as well, provided the associated analytical expressions are available.

We begin by considering two different models to represent the charged shell surface, homogeneously charged or equipotential (conducting), and carry out the ion condensation analysis for each model. For either case, the Coulomb energy of an oblate spheroid subject to the constraint of constant volume can be written in the following form

$$U(e,R,z,N) = \frac{l_B z^2 N^2}{R} f(e), \qquad \textbf{[S47]}$$

where we have used $Q = zN$, with N being the total number of charges on the shell surface. For a homogeneously charged surface, the function $f(e)$ can be deduced from Eq. **S44** to be

$$f(e) = \frac{(1-e^2)^{\frac{1}{6}}}{(S(e))^2}\frac{i}{e} \times \sum_{n=0,2,4,\ldots} \frac{2n+1}{2} Q_n\left(i\frac{\sqrt{1-e^2}}{e}\right) P_n\left(i\frac{\sqrt{1-e^2}}{e}\right) (I_n(e))^2, \qquad \textbf{[S48]}$$

and for a conducting surface, we have from ref. 6

$$f(e) = \frac{(1-e^2)^{\frac{1}{6}}}{2e}\tan^{-1}\frac{e}{\sqrt{1-e^2}}. \qquad \textbf{[S49]}$$

It can be checked that $f(e) = 1/2$ for a spherical shell and it decreases as e is increased, approaching the value of 0 as $e \to 1$. Recall that the latter case corresponds to a disc of infinitely large area and so the vanishing of the electrostatic energy in that limit gets justified. We again define the electrostatic energy difference dU as

$$dU(e,R,z,N) = U(e,R,z,N) - U(e\to 0,R,z,N) \qquad \textbf{[S50]}$$

and introduce the free-energy difference dF,

$$dF(e,R,z,N) = F(e,R,z,N) - F(e\to 0,R,z,N), \qquad \textbf{[S51]}$$

where F is the free energy (that includes the entropy contribution of condensed and free ions) of the shell. We study how dF and dU are modified when the possibility of counterion condensation is included in the analysis.

Let α be the fraction of counterions that condense. Clearly, $(1-\alpha)N$ ions remain free in the bulk. Further, the condensed ions neutralize the surface charge on the shell reducing the net charge to $Q = z(1-\alpha)N$. We approximate the WS cell to be spherical with volume $V_{\rm WS} = (4/3)\pi R_{\rm WS}^3$, with $R_{\rm WS}$ being the radius of the cell that gets determined by the shell volume fraction. We write the free energy (in units of k_BT) associated with the shell as

$$F(\alpha) = \frac{l_B z^2 N^2 (1-\alpha)^2 f(e)}{R} + \alpha N \ln\left(\frac{\alpha N \Lambda^3}{2\pi a^2 S(e) b}\right) - \alpha N + (1-\alpha)N \ln\left(\frac{(1-\alpha)N\Lambda^3}{\frac{4}{3}\pi R_{\rm WS}^3}\right) - (1-\alpha)N, \qquad \textbf{[S52]}$$

where Λ is the thermal de Broglie wavelength and we have suppressed the dependence of F on other variables for the sake of brevity. In Eq. **S52**, the first term is the electrostatic potential energy of the shell with charge $z(1-\alpha)N$, the next two terms stem from the entropic contribution of the αN condensed ions, and the last two terms correspond to the entropy of $(1-\alpha)N$ free counterions. Note that within this model, the entropy of both the condensed and free ions is assumed to be that of an ideal gas. Further, note that a is a function of e and R and is given by Eq. **S43**. We approximate the thickness b of the condensed layer by the Gouy–Chapman (GC) length $b = 1/(2\pi l_{\rm B}\sigma)$, where σ is the shell charge density (5). Higher charge density or longer Bjerrum length leads to a stronger shell–counterion attraction implying a thin condensed layer; this is indeed reflected when b is chosen as the layer thickness as seen from the above expression. We also note that the GC length is a length scale associated with the planar interface and hence our analysis is limited to the regime where b is shorter than the characteristic lengths associated with the shell. We have carried out the following analysis by choosing the Bjerrum length $l_{\rm B}$ as the thickness of the condensed layer and we find no changes in the conclusions reached below.

As σ is a function of the area, which depends on e, the free energy F in Eq. **S52** can be considered as a function of e and α. For a given e, we now minimize the above free energy with respect to α to find the fraction of counterions that condense on the shell. We obtain the extremum condition

$$-\xi(1-\alpha) + N\ln\left(\frac{\alpha}{1-\alpha}\frac{2}{3}\frac{\lambda}{\eta}\frac{(1-e^2)^{\frac{1}{2}}}{S(e)}\right) = 0, \qquad \textbf{[S53]}$$

where $\xi = 2l_B z^2 N^2 f(e)/R$ measures the strength of the Coulomb interactions, $\lambda = a/b$ can be considered as the Manning length associated with the shell, and η is the volume fraction of the shells given by

$$\eta = \frac{\Omega}{V_{\rm WS}} = \frac{\frac{4}{3}\pi R^3}{\frac{4}{3}\pi R_{\rm WS}^3}. \qquad \textbf{[S54]}$$

We note that in the limit $e \to 0$, λ becomes the Manning radius of the sphere (5).

We now compute the condensed fraction for the example studied in previous section that corresponds to our simulations. We take $R = 10$ nm, $z = 0.6$, and $n = 1{,}000$. We begin with the case of a homogeneously charged shell surface using $f(e)$ from Eq. **S48** in Eq. **S53**. For a given e and η, we solve Eq. **S53** using Mathematica (Wolfram). We obtain α as a function of e for various values of shell volume fractions ranging from 10^{-12} to 10^{-3}. We find that α decreases with increasing e for all values of η. That is, higher the eccentricity of the shell, lower is the amount of ion condensation on it. Further, α is lowest in the dilute limit when η is very small (10^{-12}), and it increases as the volume fraction gets larger. Using the value of α, the electrostatic energy $\overline{U}$ of the shell at equilibrium can be computed from Eq. **S47** by replacing N with $(1-\alpha)N$:

$$\overline{U} = \frac{l_B(1-\alpha)^2 z^2 N^2}{R} f(e). \qquad \textbf{[S55]}$$

Using the above result in Eq. **S50**, the difference between the renormalized electrostatic energy of the oblate shell and that of the sphere, dU, can be calculated. It is easy to show that the free-energy difference, dF, defined in Eq. **S51**, at equilibrium is given by

$$dF = \frac{1+\alpha}{1-\alpha}\overline{U} - \frac{1+\alpha_s}{1-\alpha_s}\overline{U}_s + N\ln\frac{1-\alpha}{1-\alpha_s}. \qquad \textbf{[S56]}$$

In Eq. **S56**, α is the fraction of condensed counterions on the shell (obtained as the solution of Eq. **S53**) and $\overline{U}$ is given by **[S55]**. α_s and $\overline{U}_s$ denote these values for the case of a spherical shell.

In Fig. S4, we plot dF computed from Eq. **S56** as a function of e for various values of η. We consider e values from 0 to 0.95 and examine if the sphere-to-oblate shape transitions are favorable within this range of eccentricity values according to the analysis based on the two-state model. The red line corresponds to the case of no ion condensation and provides a reference. All other lines are the result of taking ion condensation into consideration and correspond to different values of η ranging from 10^{-12} to 10^{-3}. We find that for all values of the volume fraction η, dF becomes increasingly more negative as the eccentricity e is raised, implying that the shape transitions from sphere to oblate spheroids are favored. We examine each of these curves in greater detail. The lower values of shell volume fraction, $\eta = 10^{-12}$ (green), 10^{-11} (blue), and 10^{-10} (dark green) correspond to a dilute system, and we find that the dF curves for these volume fractions lie in the vicinity of the no-condensation result. We find the condensate fraction α for these η values to be near 0.1. For slightly higher values of packing fraction, $\eta = 10^{-8}$ (brown) and 10^{-6} (orange), which we will term as intermediate values, we obtain the condensate fraction to be around 0.3. Finally, for higher shell volume fractions, $\eta = 10^{-4}$ (purple) and 10^{-3} (cyan), we obtain α to be ~0.5, implying the condensation of nearly half of the counterions in the WS cell. To summarize, we find that for both low and high amounts of condensation, the shell with higher eccentricity is preferred energetically.

Next, in Fig. S5 we show the variation of dU with e for different η values to probe the origin of these shape transitions. When the volume fraction is low ($\eta = 10^{-12}$ and 10^{-11}), we find that dU is negative and decreases (just like dF) upon the increase of e. We find a similar trend for higher values of η (10^{-4} and 10^{-3}), where the behavior of dU is in alignment with the free-energy change dF. However, for $\eta = 10^{-10}$ and the intermediate values of $\eta = 10^{-8}$ and 10^{-6}, we observe that the variation of dU vs. e is in sharp contrast with the corresponding results for dF. For example, in the case of $\eta = 10^{-10}$ (the dashed dark-green line), we find that oblates of eccentricities closer to 0 (sphere-like) have a higher energy than a sphere ($e = 0$), but the high eccentricity oblate spheroids have lower energy than a sphere. Further, for $\eta = 10^{-8}$ and 10^{-6}, we find that the electrostatic energy increases as e is raised in sharp contrast to the free energy associated with the shell. We can understand this by observing the expression for the equilibrium electrostatic energy $\overline{U}$ given by Eq. **S55**. As we noted before, α decreases with increasing e for all values of η implying that the factor $(1-\alpha)^2$ rises as e increases. On the other hand, the function $f(e)$, given by Eq. **S48**, is a monotonically decreasing function of e as is evident from the plot of dU in Fig. S2. For some values of η, the decrease in α with increase in e is strong enough to overcome the lowering of $f(e)$, thus leading to the rise in the renormalized electrostatic energy $\overline{U}$ as the shape is transformed from a sphere to an oblate.

The main conclusions reached above remain unchanged when we repeat the two-state model analysis assuming that the shell is an equipotential surface. This calculation begins by using $f(e)$ given by Eq. **S49** in Eq. **S53** and solving for the condensate fraction α. Once again we find that, for all values of η, α decreases and dF becomes increasingly more negative as the eccentricity e is raised, implying that the shape transitions from sphere to oblate spheroids are favored. We present these findings in Fig. S6. We also observe that for all values of η, the reduction in the free energy of the shell upon deformation to an oblate shape is higher for a conducting shell in comparison with the homogeneously charged shell. We show the comparison for the particular value of $\eta = 10^{-8}$ in Fig. S6, *Inset*.

Thus, judging by the variation of dF vs. e determined by the above two-state model analysis, we conclude that if the shell is flexible enough, the shape transitions from sphere to oblates of increasing eccentricity should be feasible in the event of ion condensation. However, due to the renormalization of the charge on the shell surface as a result of the ion condensation, it is likely that the specific parameter values (for example, the concentration strengths) at which the shape transitions occur will change. Also, as is evident from Fig. S5, we find that the transition to oblate shapes will not always accompany a decrease in the electrostatic energy. For some values of shell volume fractions, the transition will occur despite an increase in the electrostatic energy. We attribute the occurrence of such transitions to the entropy gained by the ions due to the reduction in the number of ions that condense when the shape is deformed from a sphere to an oblate.

1. Ciftja O, Hysi I (2011) The electrostatic potential of a uniformly charged disk as the source of novel mathematical identities. *Appl Math Lett* 24(11):1919–1923.
2. Oosawa F (1971) *Polyelectrolytes* (Marcel Dekker, New York).
3. Manning GS (2007) Counterion condensation on charged spheres, cylinders, and planes. *J Phys Chem B* 111(29):8554–8559.
4. Borukhov I (2004) Charge renormalization of cylinders and spheres: Ion size effects. *J Polym Sci, B, Polym Phys* 42(19):3598–3615.
5. Gillespie DAJ, et al. (2014) Counterion condensation on spheres in the salt-free limit. *Soft Matter* 10(4):566–577.
6. Landau LD, Lifshitz EM (1984) *Electrodynamics of Continuous Media* (Pergamon, New York).

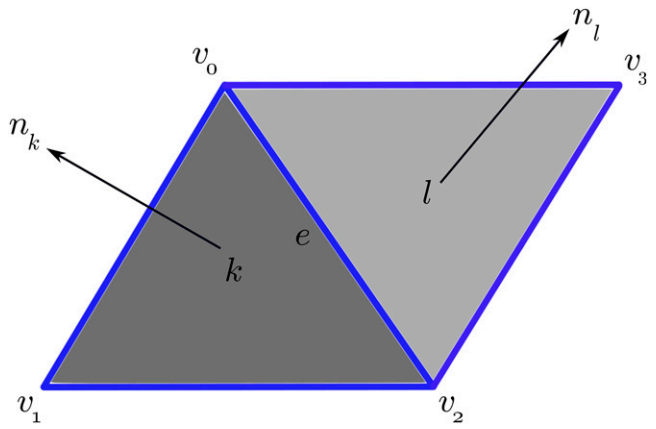

Fig. S1. Edge *e* shared by the faces *k* and *l* shown along with their associated normals. Vertices v_0 and v_2 belong to the edge *e* whereas the vertices that do not lie on *e* are v_1 and v_3. The dot product of the normals is a function of the position vectors of all four vertices. The bending energy gradient evaluation with respect to a vertex that belongs to the shared edge (v_0 or v_2) is different from the evaluation with respect to the vertex that is not a part of the shared edge (v_1 or v_3).

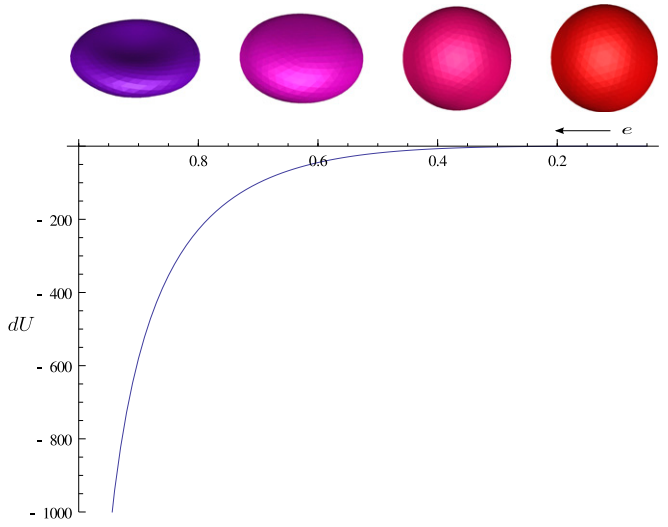

Fig. S2. Electrostatic energy difference *dU* in units of k_BT between an oblate spheroidal shell and a sphere of identical parameters ($Q = 600$ and $R = 10$ nm) as a function of the eccentricity *e*. *e* increases from right to left. The oblate shell has a lower energy than the spherical shell with the difference increasing with increasing *e*. This figure qualitatively captures the trend of the electrostatic energy represented by the blue open circles in Fig. 3. The snapshots of the shell shapes obtained in the simulations corresponding to the above parameters as a result of lowering concentration (from right to left) appear at top.

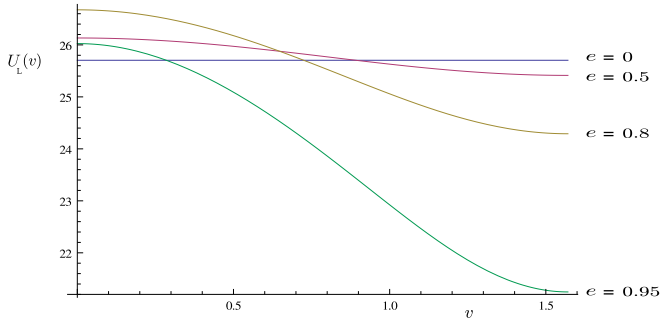

Fig. S3. Local electrostatic potential energy $U_L(v)$ on the shell surface (in units of k_BT) as a function of the oblate spheroidal coordinate *v* for spheroidal shells of different eccentricities *e*. The coordinate *v* measures the angular deviation from the *z* axis, the latter being taken along the minor axis of the spheroid. Thus, $v = 0$ corresponds to the center (poles) of the shell and $v = \pi/2$ refers to its edge (equator). For $e = 0$, which corresponds to the spherical shell, the potential is constant everywhere on the shell as expected. As *e* is raised, the potential becomes increasingly nonuniform. Note that shells characterized with different *e* correspond to the same volume. This figure qualitatively captures the features of the spatial distribution of electrostatic energy on the surface of a disc as reported in the top row of Fig. 4.

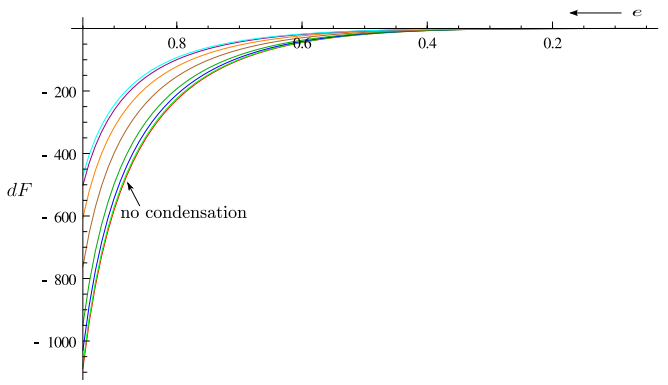

Fig. S4. Equilibrium free-energy difference dF (in units of k_BT) between an oblate spheroidal shell and a sphere of identical parameters ($z = 0.6$, $n = 1{,}000$, and $R = 10$ nm) as a function of the eccentricity e assuming the shell to be a homogeneously charged surface postcondensation. The red curve is the case when we assume no counterion condensation on the shell surface. All other curves take into account ion condensation and correspond to different values of the shell volume fraction η. Results are shown for $\eta = 10^{-12}$ (green), 10^{-11} (blue), 10^{-10} (dark green), 10^{-8} (brown), 10^{-6} (orange), 10^{-4} (purple), and 10^{-3} (cyan). We find that the oblate shell has a lower free energy than the spherical shell with the difference enhancing as e increases. This suggests that the shape transition from a sphere to an oblate spheroid is feasible in the event of ion condensation.

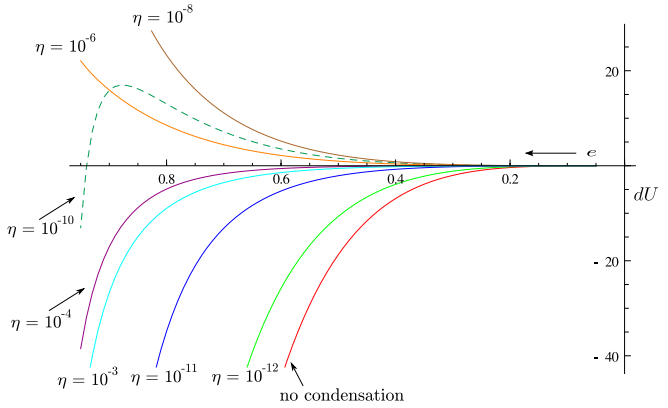

Fig. S5. Equilibrium electrostatic energy difference dU (in units of k_BT) between an oblate spheroidal shell and a sphere of identical parameters ($z = 0.6$, $n = 1{,}000$, and $R = 10$ nm) as a function of the eccentricity e. Here, the shell is assumed to be a homogeneously charged surface postcondensation. The red curve is the case when we assume no counterion condensation on the shell surface. All of the other curves take into account ion condensation and correspond to different values of the shell volume fraction η. η values are shown alongside each curve.

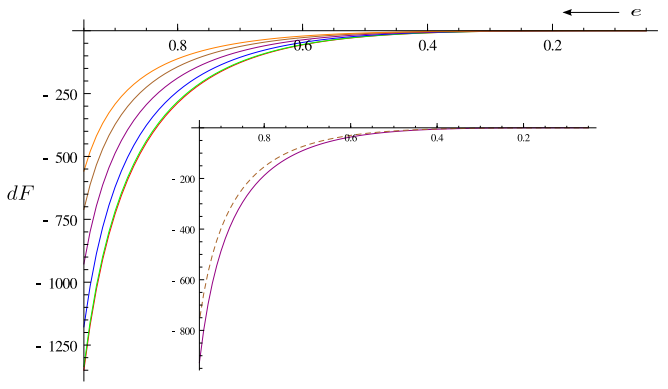

Fig. S6. Equilibrium free-energy difference dF (in units of k_BT) between an oblate spheroidal shell and a sphere of identical parameters ($z = 0.6$, $n = 1{,}000$, and $R = 10$ nm) as a function of the eccentricity e. Here, the shell is assumed to be an equipotential surface postcondensation. The red curve is the case when we assume no counterion condensation on the shell surface. All other curves take into account ion condensation and correspond to different values of the shell volume fraction η. Results are shown for $\eta = 10^{-12}$ (green), 10^{-10} (blue), 10^{-8} (purple), 10^{-6} (brown), and 10^{-4} (orange). We find that the oblate shell has a lower free energy than the spherical shell with the difference enhancing as e increases. This suggests that the shape transition from a sphere to an oblate spheroid is feasible in the event of ion condensation. *Inset* shows the comparison between dF obtained by assuming a homogeneously charged shell (dashed line) vs. a conducting shell (solid line) in the two-state model analysis for $\eta = 10^{-8}$.